JOURNAL OF AIRCRAFT
Vol. 53, No. 4, July-August 2016

Multi-Element Winglets: Multi-Objective Optimization of Aerodynamic Shapes

Sohail R. Reddy*
Florida International University, Miami, Florida 33174
Helmut Sobieczky†
Vienna University of Technology, 1010 Vienna, Austria
and
George S. Dulikravic‡ and Abas Abdoli§
Florida International University, Miami, Florida 33174

DOI: 10.2514/1.C033334

The wing tip device in this study was to mimic the wing tips of a soaring bird, featuring three smoothly blended elements. Each such multi-element winglet was integrated into a complete wing–tail–body aircraft configuration. The geometry of each of the three elements in the multi-element winglet was defined using 11 parameters, totaling 33 parameters for a complete multi-element winglet geometry. This design methodology used a three-dimensional geometry generation algorithm based on locally analytical smoothly connected surface patches, allowing for the creation of vastly diverse three-dimensional geometries with a minimal number of specified design parameters. A three-dimensional, compressible, turbulent flow, steady-state analysis was performed using a Reynolds-averaged Navier–Stokes solver on each configuration to obtain the objective function values. Each configuration was analyzed at a freestream Mach number of 0.25 and at an angle of attack of 11 deg to mimic the takeoff conditions of a passenger aircraft. Multi-objective optimization was carried out using modeFRONTIER, using a radial basis function response surface approximation coupled with a genetic algorithm. Maximizing coefficients of the lift and lift-to-drag ratio and minimizing the coefficients of drag and the magnitude of the coefficient of the moment were the four simultaneous objectives. The Pareto-optimized multi-element winglet concept demonstrated superior performance at subsonic and transonic speeds.

Nomenclature

C_l	=	aerodynamic lift coefficient
C_d	=	aerodynamic drag coefficient
C_m	=	pitching moment coefficient
C_l/C_d	=	lift-to-drag ratio
L.E.S.	=	leading-edge sweep angle, deg
T.E.S.	=	trailing-edge sweep angle, deg
τ	=	relative thickness of the local airfoil
θ_f	=	angle of geometric parameter f, deg
α	=	angle of attack, deg
$y+$	=	y-plus distance in turbulent flow calculations

I. Introduction

A CONSTANT increase in jet fuel costs has motivated the aerospace field to search for innovative methods to improve aerodynamic efficiency. This eventually led to the invention of wing-tip devices called winglets in order to reduce aerodynamic drag. The pressure difference between the upper and lower surfaces of the wing tries to equalize itself at the wing tips, causing trailing vortices that create induced drag. These wing-tip devices have been implemented in an effort to break down trailing vortices, thereby reducing the induced drag, which is greatest in high lift scenarios such as takeoff and landings of aircraft but is also significant over the longer cruise segments.

The aerodynamic induced drag is inversely proportional to the radii of the vortices and the spacing between them [1]. The amount of drag induced by an aircraft can be significantly reduced by implementing a wing-tip design that increases the radii of the vortices and the distance between the vortices [2]. Since the first patented wing tip device in 1910, winglets have continued to evolve. What started off as the classical and popular blended horns-up configuration, winglets [3] have now evolved into the split-scimitar winglets [4,5] that have yet another element attached. Along the way, various nontraditional configurations have also been implemented such as the spiroid winglets [6] and the wing-tip fence. The authors have shown [4,5] that the optimized scimitar winglets offer a significant improvement in performance over the optimized blended winglets using numerical analysis validated by experimental results. The optimized scimitar winglets have shown a 4% decrease in drag, a 23% decrease in the pitching moment, and a 3% increase in lift over the blended winglets. This addition of the secondary lower element has also shown to improve aerodynamic stability even in the poststall flight condition.

This addition of elements forms a trend in future winglet technology mimicking a bird's wing-tip feathers. The effects of various configurations of feather winglets or multi-element winglets have been experimentally analyzed [7,8], which would be prohibitively expensive when performing design optimization. This was overcome in the present study by using computational methods. The multi-element winglet configurations in this study, shown in Fig. 1b, featured a three-element winglet, smoothly retrofitted to the wing tips of a wing–tail–body configuration. Figure 1a shows the wing–tail–body configuration used for each winglet configuration analysis. It should be mentioned that the wing–tail–body configuration used to analyze each winglet configuration is by no means aerodynamically optimized. That is, the performance of each winglet design should be measured relative to other wing-tip configurations.

Single, horns-up winglets have previously been optimized for various applications. A combined inverse design and optimization approach was presented by Kubrynski [9], resulting in award-winning sailplanes. This, however, requires the user to be an experi-

Presented as Paper 2015-1489 at the 53rd AIAA Aerospace Sciences Meeting, Kissimmee, FL, 5–9 January 2015; received 2 January 2015; revision received 22 June 2015; accepted for publication 10 September 2015; published online 9 November 2015.

*Graduate Research Assistant, Department of Mechanical and Materials Engineering. Student Member AIAA.
†Professor, Institute of Fluid Mechanics and Heat Transfer. Fellow AIAA.
‡Professor, Director of MAIDROC Laboratory, Department of Mechanical and Materials Engineering. Associate Fellow AIAA.
§Graduate Research Assistant, Department of Mechanical and Materials Engineering; currently Postdoctoral Research Associate, University of Miami, Medical School.

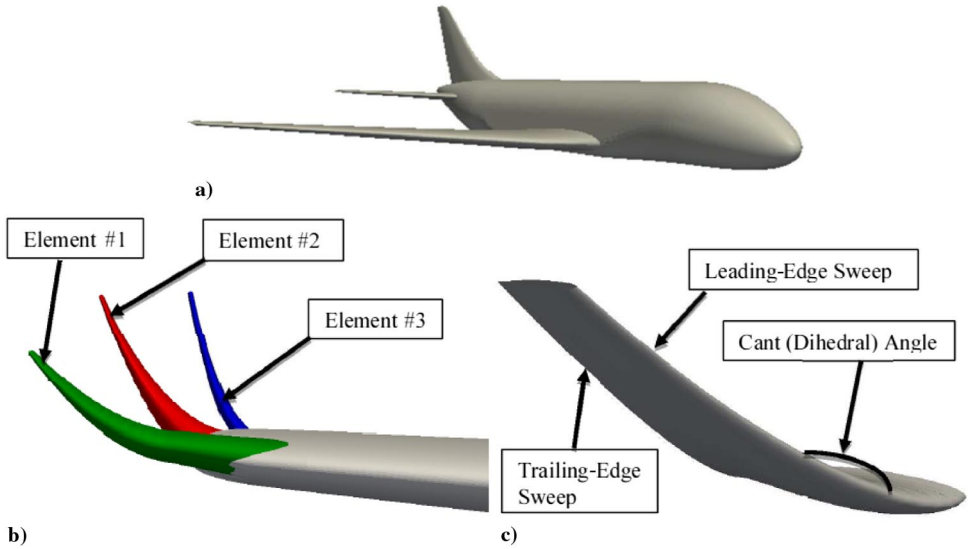

Fig. 1 a) The wing–tail–body configuration used to analyze each winglet design, b) the three elements used for each winglet geometry, and c) some of the parameters used to define each winglet element.

enced aerodynamicist due to the requirement to prescribe good pressure distribution on such winglets when performing an inverse shape design. Multidisciplinary and multi-objective optimization has been carried out on single winglets by Takenake et al. [10], Ursache et al. [11], and Minella et al. [12]. Weierman and Jacob [13] previously optimized blended winglets for unmanned aerial vehicle and EnginSoft for the Piaggio Aero business jet [14]. Various winglet geometries have also previously been numerically investigated by Bourdin et al. [15] and recently by Gavrilovic et al. [16].

Most of the efforts make use of arbitrary configurations that only investigate a small aspect of the geometry. This study introduces more parameters, shown in Fig. 1c, to investigate a more complete configuration. Each winglet configuration was analyzed using the OpenFOAM [17] computational fluid dynamics platform, while the optimization was performed using modeFRONTIER [18] software with radial basis functions based response surface approximations coupled with a multi-objective optimizer based on a genetic algorithm.

II. Geometry Definition

An efficient method to define the geometry is very appealing when performing aerodynamic shape design optimization. A method that defines the geometry with a minimum number of parameters (design variables) greatly reduces the computational cost. A flexible geometry generator with minimal input drastically reduces the number of design variables, thus requiring a smaller initial population needed to create a response surface [19] for each of the objective functions. This study uses FORTRAN code E300 developed by Klein and Sobieczky [20] and Sobieczky [21]. It uses stored analytical functions defined over subintervals to define the three-dimensional (3-D) surface. A smooth piecewise composition of these analytical functions yields a continuous curve with the user maintaining complete control over each subinterval. A three-dimensional composition of these curves can be used to control the extrusion of a cross-section as shown in Fig. 2. The entire wing–tail–body configuration was created using this software, which insures C2-continuity between adjacent surface analytical patches and requires maximum flexibility by varying the minimal number of input parameters.

Multiple winglets were generated using a different analytical formulation that required only 33 input parameters to fully define the shapes and sizes of each of the three-element winglets.

These geometric parameters include those defining the leading- and trailing-edge sweep angles, cant angle, twist angle, relative thickness, and span of each of the three winglet elements. Controlling the leading-edge and trailing-edge sweep independently allows for control of the taper ratio. A symmetric PARSEC11 airfoil was used to define each element of the multi-element winglet geometry.

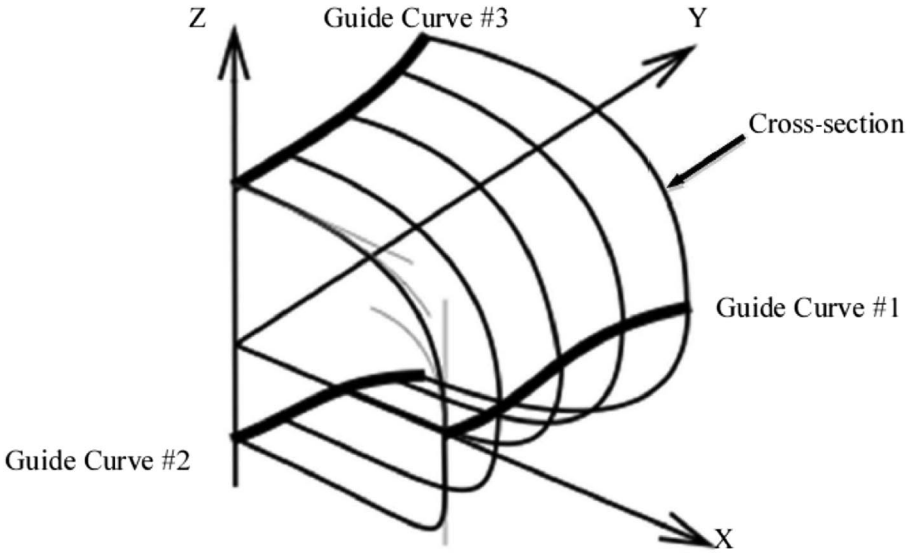

Fig. 2 Surface definition using multiple guide curves.

The leading-edge and trailing-edge sweeps, cant angle, twist, and relative thickness were allowed to vary in the spanwise direction as a simple third-order polynomial as shown in Eq. (1),

$$f_K = a_K S_K^3 + b_K S_K^2 + c_K S_K + d_K \tag{1}$$

where the normalized spanwise distance from the winglet root to tip of the Kth winglet element is given as

$$S_K = (s_K - s_{\text{root}K})/(s_{\text{tip}K} - s_{\text{root}K}) \tag{2}$$

At the root of Kth ($S_K = 0$) winglet element, the following two conditions must be satisfied:

$$f_{\text{root}K} = d_K = d_{\text{root}K} \tag{3}$$

$$\left.\frac{\mathrm{d}f}{\mathrm{d}S}\right|_{\text{root}K} = 0 = c_K \tag{4}$$

At the tip of Kth ($S_K = 1$) winglet element, the following two conditions must be satisfied:

$$f_{\text{tip}K} = a_K + b_K + c_K + d_K \tag{5}$$

$$\left.\frac{\mathrm{d}f}{\mathrm{d}S}\right|_{\text{tip}K} = 3a_K + 2b_K + c_K \tag{6}$$

It is evident from Eqs. (3–6) that

$$b_K = -\left.\frac{\mathrm{d}f}{\mathrm{d}S}\right|_{\text{tip}K} + 3(f_{\text{tip}K} - f_{\text{root}K}) \tag{7}$$

$$a_K = \left.\frac{\mathrm{d}f}{\mathrm{d}S}\right|_{\text{tip}K} - 2(f_{\text{tip}K} - f_{\text{root}K}) \tag{8}$$

Defining the spanwise variation in this manner allows for the control of each of the five parameters (leading-edge and trailing-edge sweeps, cant angle, twist angle, and relative thickness) by varying $f_{\text{tip}K}$, $f_{\text{root}K}$, and $(\mathrm{d}f/\mathrm{d}S)_{\text{tip}}$. To allow for a smooth transition between the wing tip and the root of the winglet element and to prevent the intersection of individual winglet elements, the values ($f_{\text{root}K}$) of each of the five parameters for each winglet element were kept constant. These fixed parameters at the root of each of the three winglet elements are shown in Table 1.

III. Aerodynamic Analysis

The objective functions (coefficients of lift, drag, lift-to-drag ratio, and pitching moment) for each winglet configuration were obtained by carrying out 3-D fluid flow analysis in the OpenFOAM [17] software platform. OpenFOAM makes use of Gaussian finite-volume integration over hexahedral cells for the computation of derivatives. OpenFOAM's compressible flow solver, rhoSimpleFoam, was used to perform all aerodynamic analysis. This solver uses the SIMPLE algorithm for the velocity–pressure coupling and was extensively validated by Rahman and Mustapha [22]. Their work shows that the results obtained from the rhoSimpleFoam solver are in good agreement with the experimental results. The standard κ-ε turbulence model was used to capture vortex shedding and flow separation, with standard no-slip and no-penetration boundary conditions at the solid surfaces. The standard κ-ε turbulence model was implemented by Ashrafi and Sedaghat [23] in their work to improve the aerodynamic performance of an isolated wing with a horns-up winglet. Their work also showed good agreement with the experimental data.

A boundary-conforming computational grid of approximately 42 million grid cells was used in the present work for each of the randomly generated three-element winglet configurations. The wing–tail–body configuration was kept unchanged during the optimization process of the three-element winglet shape. The generation of a computational grid of hexahedral grid cells was performed using two built-in grid generators for OpenFOAM. To grid the fluid domain, blockMesh was first used. Then, the snappyHexMesh utility was used to refine the grid around the aircraft geometry.

Table 1 Fixed parameters at the winglet elements' roots to avoid intersection

Parameter	Element #1	Element #2	Element #3
$\text{Twist}_{\text{Root}}$, deg	0	0	0
Relative $\text{thickness}_{\text{Root}}$, %	15	30	10
Chord $\text{length}_{\text{Root}}$, m	1.3	0.8	0.85

Computational grid generation for each case took approximately 4 h. A single processor was used for each case, with 15 GB RAM allocated per case. Each 3-D aerodynamic analysis run took approximately 41 h when starting with a uniform flow. A grid refinement convergence study was performed, in which the grid size of 42 million grid cells no longer changed the solution or the four aerodynamic coefficients, thereby confirming that numerical results will be independent of the grid size if using at least 42 million grid cells.

As performance benefits of various winglet configurations are analyzed, a benchmark value is needed for comparison. For this reason, a basic wing–tail–body configuration, without winglets, was analyzed at a freestream Mach number of 0.25 and an angle of attack of 11 deg. Although flow at the freestream Mach number less than 0.3 is often treated as incompressible, the local Mach number exceeds 0.3 at a number of locations on such a 3-D realistic airplane configuration. For this reason, a compressible, fully 3-D, turbulent

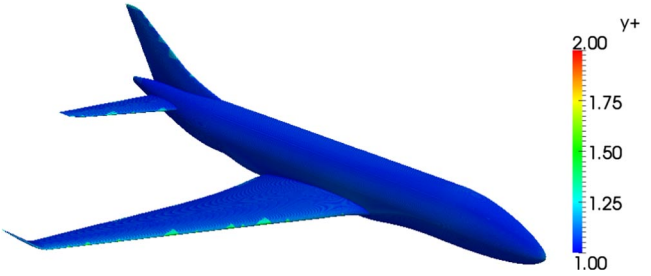

Fig. 3 $y+$ values for a typical computational grid of approximately 42 million cells used for each aerodynamic analysis. Approximately 30 cells were placed within the viscous boundary layer.

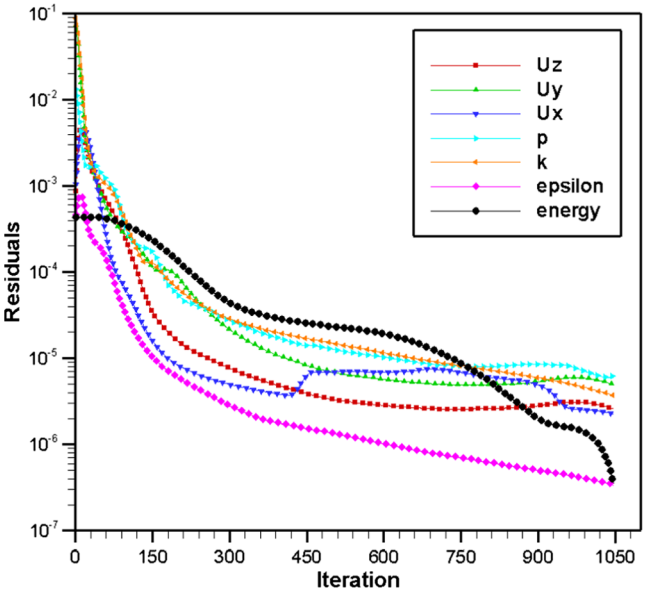

Fig. 4 A typical convergence history of OpenFOAM 3-D aerodynamic analysis software.

flow analysis solver that solves Reynolds-averaged Navier–Stokes (RANS) equations was used. Figure 3 shows the $y+$ values at the solid surface for a typical computational grid used in this study. It can be seen that the $y+$ values were very close to 1 over most of the aircraft surface, indicating a satisfactory capture of the turbulent boundary layer on such a fully 3-D configuration. Figure 4 represents a typical convergence history for 3-D analysis runs in this study. It can be concluded that the OpenFOAM aerodynamic analysis software converged fully, leading to high-fidelity values of the four objective functions. The validity of the 3-D RANS compressible flow solver used in this study has previously been confirmed by the authors, with maximum objective functions values deviating less than 5% from the experimental values [5,22].

A Trefftz plane perpendicular to freestream was placed four chord lengths downstream of the wing's trailing edge, to visualize the low-pressure region due to the wing tip vortex. Shade variation along the streamlines indicates the velocity magnitude along those streamlines. Figure 5b shows that the radius of the trailing vortex core is quite small as compared to the design incorporating winglets, as will be seen in the following figures.

The trailing vortices, shown in Fig. 5b, increase the induced drag. A nonoptimized configuration of the three-element winglet was attached to the baseline wing tip to investigate its ability to weaken these wing-tip vortices. Figure 6 shows the effects of multi-element winglets on the wing-tip vortices, whereby the minimum pressure in the Trefftz plane has increased and is now dispersed over a greater area. Figure 7 shows the streamlines around the wing tip of this configuration. Notice that, unlike in Fig. 5b, the vortices are not clustered. This shows that even a nonoptimized multi-element winglet

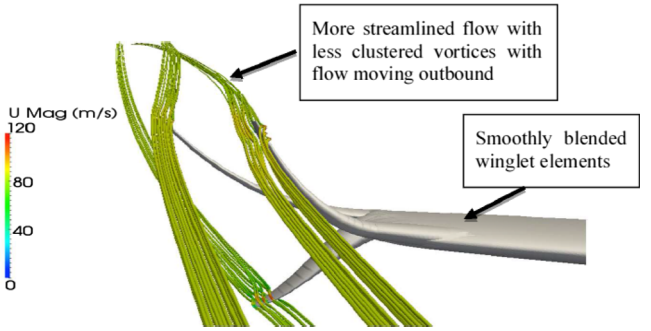

Fig. 7 Streamlines around a nonoptimized three-element winglet geometry (U Mag, velocity magnitude).

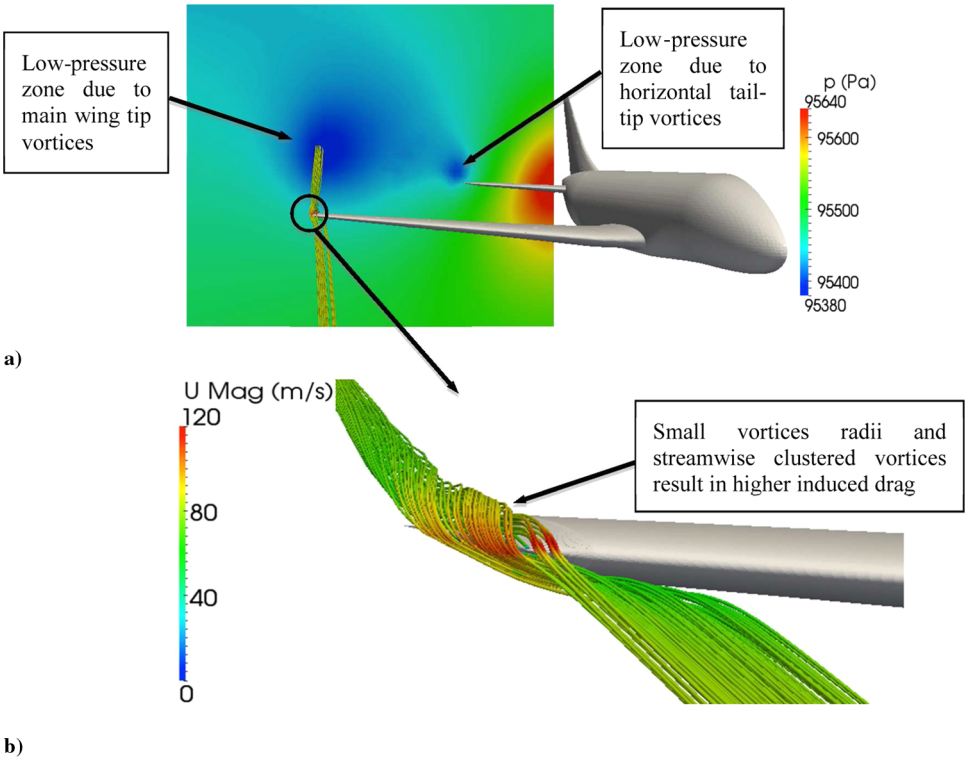

Fig. 5 a) Low-pressure region due to vortices around a baseline wing, depicted at four chord lengths downstream and b) streamlines around the wing tip of the baseline wing used in this study (U Mag, velocity magnitude; p, pressure).

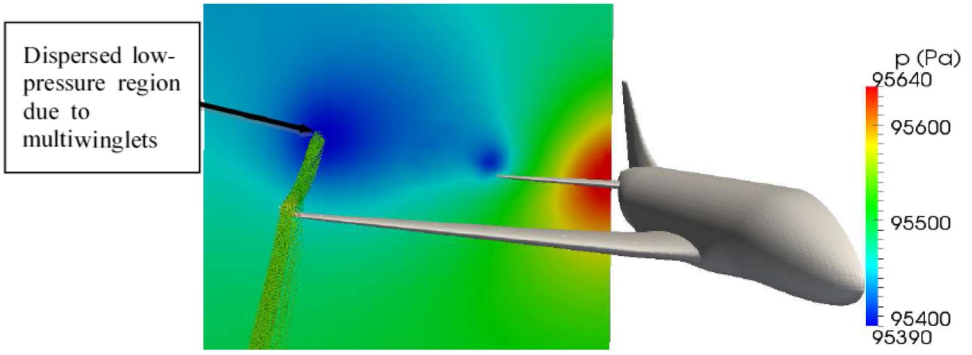

Fig. 6 Low-pressure region due to vortices around a nonoptimized three-element winglet geometry, depicted at four chord lengths downstream from the wing-tip trailing edge (p, pressure).

configuration is effective in reducing the induced drag. The multi-objective shape design optimization, that were consequently performed on this conceptual three-element winglet attached to the wing–tail–body configuration, has led to significant improvements in aerodynamic performance over the nonoptimized configuration of the three-element winglet.

IV. Optimization

The multi-objective optimization of the multi-element winglet shape was carried out using a commercial software package modeFRONTIER [18]. The following are the 11 design variables considered for each of the multi-element winglet elements: 1) span S, 2) twist angle θ_{Twist}, 3) variation of the twist angle in the span direction $d\theta_{\text{Twist}}/dS$, 4) leading-edge sweep angle $\theta_{\text{L.E.S}}$, 5) variation of the leading-edge sweep angle in the span direction $d\theta_{\text{L.E.S}}/dS$, 6) trailing-edge sweep angle $\theta_{\text{T.E.S}}$, 7) variation of the trailing-edge sweep angle in the span direction $d\theta_{\text{T.E.S}}/dS$, 8) cant (dihedral) angle θ_{Cant}, 9) variation of the cant angle in the span direction $d\theta_{\text{Cant}}/dS$, 10) relative thickness of the local airfoil τ, and 11) variation of the relative thickness of the local airfoil in the span direction $d\tau/dS$.

Thus, for the multi-element winglet with three elements, the total number of designs variables was 33. Since each 3-D aerodynamic analysis was computationally time consuming, the use of metamodels is very appealing. For this reason, a 33-dimensional (since there were 33 geometric design variables in this study) response surface approximation based on the Gaussian Radial Basis Function (GRBF) was created for each of the four simultaneous objectives. It was demonstrated by Colaço and Dulikravich [19] that an optimized polynomial radial basis functions method gives consistently more accurate results as compared to other response surface methods. In the present study, the response surfaces were created using the high-fidelity values of the objective functions of the 433 geometric configurations of the three-element winglet. The accuracy of the response surfaces was verified by comparing the objective function values obtained from their interpolation and the compressible flow RANS solver. It was found that GRBF returned values within 5% error of the compressible RANS solver.

The four simultaneous objective functions in this study were as follows:

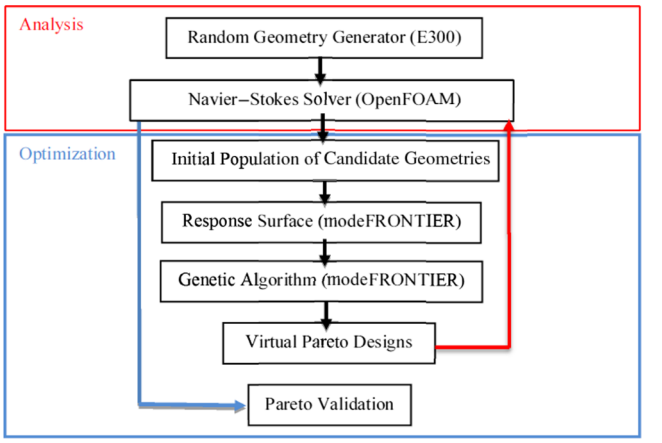

Fig. 8 Flowchart showing the coupling of different software modules.

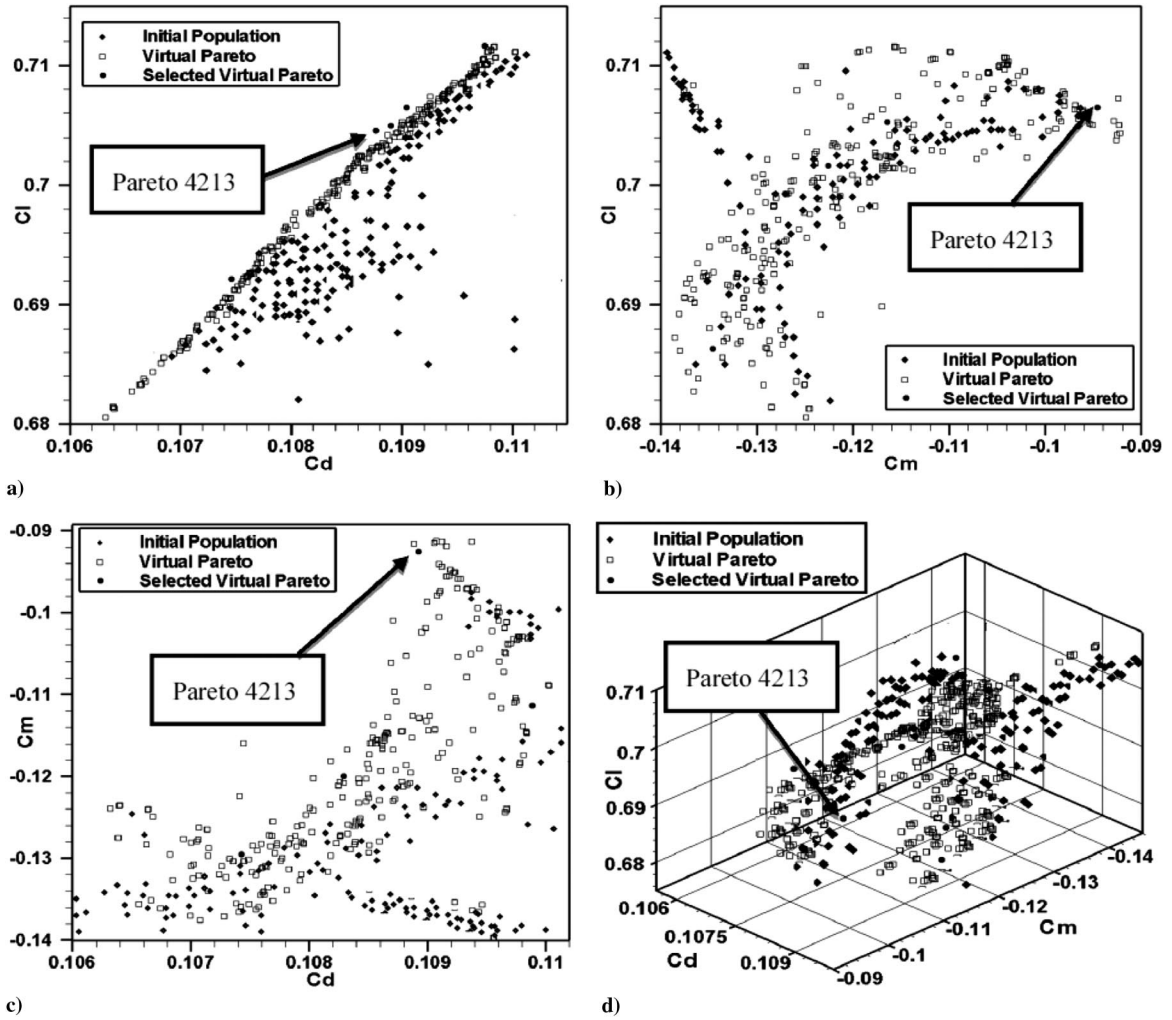

Fig. 9 Response surface points for a) C_l vs C_d, b) C_l vs C_m, c) C_m vs C_d, and d) the objective function space of C_l vs C_d vs C_m for the initial population and for virtual Pareto-optimized designs.

1) Maximize the lift coefficient of the entire wing–winglet–body–tail configuration.
2) Maximize the lift-to-drag ratio of the entire wing–winglet–body–tail configuration.
3) Minimize the drag coefficient of the entire wing–winglet–body–tail configuration.
4) Minimize the pitching moment coefficient of the entire wing–winglet–body–tail configuration.

The response surfaces were then coupled with the genetic algorithm NSGA-II developed by Deb et al. [24,25]. The genetic algorithm searched the response surfaces to arrive at a Pareto frontier of best tradeoff solutions. The response surface construction took approximately 10 min, while the optimization took approximately 5 min and did not involve optimizing the wing–tail–body configuration.

Table 2 Pareto-optimized values of the 33 design variables defining the Pareto-optimized three-element winglet configuration 4213

Variable	Parameter	Element #1	Element #2	Element #3
1	Span, m	1.2	0.6	0.8
2	θ_{Twist}	4	−3	−2
3	$d\theta_{\text{Twist}}/dS$	0.2	2	3
4	$\theta_{\text{L.E.S}}$	13.5	45	35
5	$d\theta_{\text{L.E.S}}/dS$	1.5	2	1
6	$\theta_{\text{T.E.S}}$	20	−3	10
7	$d\theta_{\text{T.E.S}}/dS$	1	1.3	0
8	θ_{Cant}	49	70	80
9	$d\theta_{\text{Cant}}/dS$	3	0	1.5
10	τ	0.5	0.25	0.2
11	$d\tau/dS$	1.3	0	0.7

V. General Workflow of Design Methodology

The workflow used in this study is depicted in Fig. 8. The winglet geometry was efficiently parameterized, keeping the number of parameters needed to define the geometry to a minimum. A quasi-random number generator [26] was used to create the initial population of 433 candidate geometries of the three-element winglets. These were then used to create the response surfaces. Compressible, 3-D, turbulent, steady-state RANS flow analyses around each of these 433 geometries were carried out with OpenFOAM, while the multi-objective optimization was carried out with modeFRONTIER applied to the response surfaces.

VI. Results

Figure 9 depicts the initial population of candidate designs used to create the response surfaces and interpolated (virtual) Pareto designs obtained from those response surfaces. It is known that the accuracy of a response surface rapidly deteriorates outside the provided data set. For this reason, five virtual Pareto designs were randomly selected and analyzed using the RANS solver. It was found that the maximum deviation of objective function values between the response surface and the RANS solver was 4%.

In real-world applications, each winglet geometry inherits a certain degree of error during manufacturing. For this reason, each of the 30 design parameters of the five selected virtual Pareto-optimized designs were perturbed by 5% to simulate the manufacturing geometric defects. These perturbed versions of the Pareto-optimized multi-element winglets were then analyzed with the RANS solver. It was found that the Pareto 4213 optimized configuration was least sensitive to the manufacturing defects when compared to the other four Pareto-optimized designs. Consequently, three-element winglet configuration Pareto 4213 was chosen as the Pareto optimum final multi-element winglet geometry.

Figure 10 shows the streamlines around various wing tips. The flow around the blended horns-up winglet (Fig. 10b) tip is still

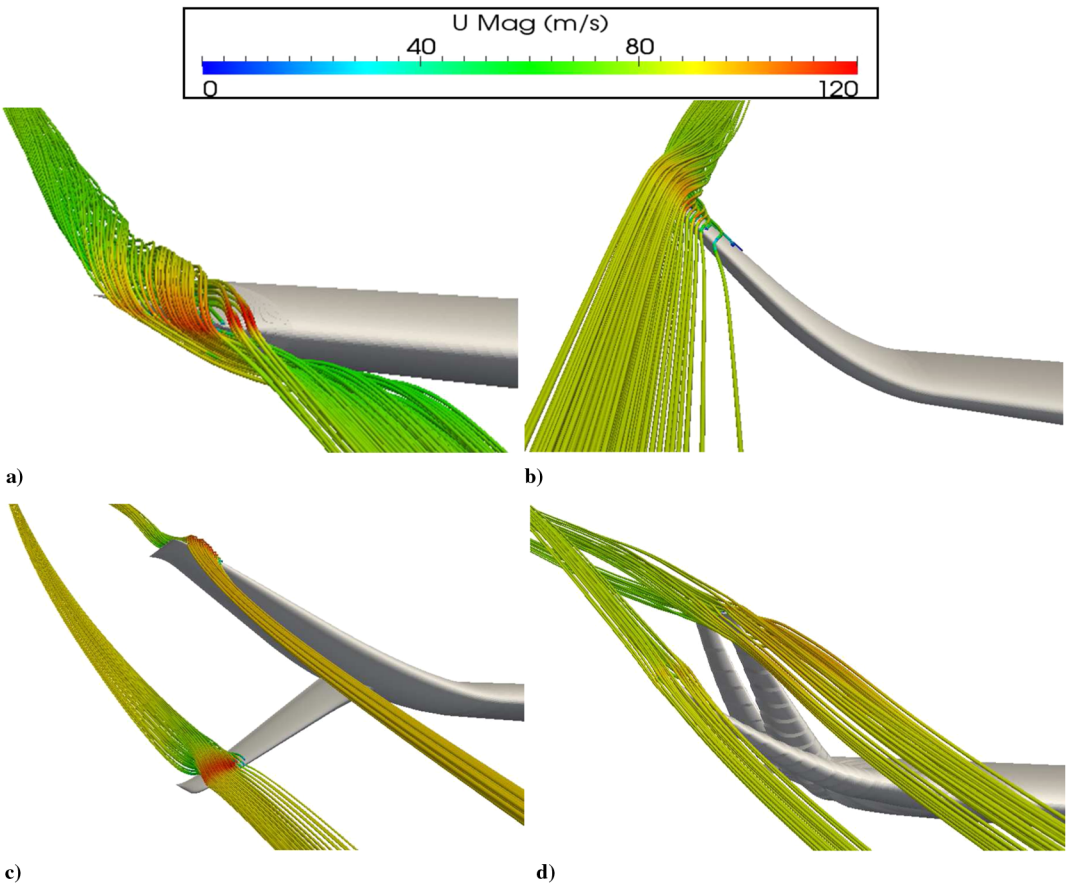

Fig. 10 Streamlines around the wing tips of a) the baseline wing, b) the blended horns-up winglet, c) the optimized split-scimitar winglet, and d) the Pareto 4213 optimized three-element winglet (U Mag, velocity magnitude).

Table 3 Objective function values and percentage improvements for various winglet configurations

Winglet configuration	C_l	ΔC_l, %	C_d	ΔC_d, %	C_m	ΔC_m, %
Baseline wing	0.630	0.00	0.110	0	−0.050	0
Optimized blended winglet	0.660	4.76	0.109	−1	−0.09	80
Optimized split-scimitar winglet	0.690	9.52	0.105	−4.5	−0.085	70
Random nonoptimized three-element winglet	0.656	4.12	0.108	−1.8	−0.088	66
Pareto optimized three-element winglet	0.711	12.80	0.105	−4.5	−0.080	60

twisted, but much less than the flow around the baseline wing tip (Fig. 10a). The optimized split-scimitar configuration [4] (Fig. 10c) created even less twisting of the flow and was better than the blended horns-up winglet (Fig. 10b). Because of the nature of this two-element winglet configuration (Fig. 10c) the counterrotating vortices from the lower element of the winglet interacted with the vortices from the upper element farther downstream. The Pareto-optimized three-element winglet configuration allowed the downstream elements of the winglet to interact with the vortices of the preceding elements (Fig. 10d). It can be seen from Figs. 7 and 10d that the flow around the tip of each element of the multi-element winglet was more streamlined due to its vortices interacting with the vortices of other elements farther upstream.

Table 2 shows the resulting values of the 33 design variables for the Pareto-optimized multi-element winglet configuration.

Table 3 demonstrates that the Pareto-optimized multi-element winglet offered significant improvements in lift and a decrease in drag. The great deviations in the coefficient of the pitching moment are due to the baseline wing stalling well before any of the configurations with winglets. The Pareto-optimized multi-element winglet has shown to decrease the coefficient of the pitching moment, while showing stable behavior at higher angles of attack.

The performance of the Pareto 4213 optimized three-element winglet, optimized split-scimitar winglet [4], optimized horns-up blended winglet [12], and the baseline wing over a range of angles of attack can be seen in Fig. 11.

It can be seen (Fig. 11) that the Pareto-optimized three-element winglet performed better than the baseline wing in all four objectives. Its performance in drag and pitching moment reduction was quite similar to that of the Pareto-optimized split-scimitar winglets. The authors have previously shown [4] the effect of wing-tip devices in delaying wing-tip stall, a phenomenon seen in Fig. 11c. It can be seen that the baseline wing suffered a catastrophic wing tip stall, shown by the rapid variation of the pitching moment. The optimized multi-element winglets and split-scimitar winglets stalled gradually and at higher angles of attack, with the Pareto 4123 geometry stalling the latest. In the operating range of the angle of attack for passenger aircraft, Pareto 4213 offered a lower coefficient of the pitching moment than the other two winglet configurations. The optimized three-element winglet also offered a significant improvement in C_l/C_D at lower subsonic speeds.

It would be very useful to verify how the baseline wing, optimized blended winglet, optimized split-scimitar winglet, and multi-element winglet (that were optimized for a freestream Mach number of 0.25) perform at transonic cruise speed.

Table 4 shows the objective function values of the four configurations analyzed at a freestream Mach number of 0.8 and an angle of attack of 5 deg to simulate the cruise conditions of the average

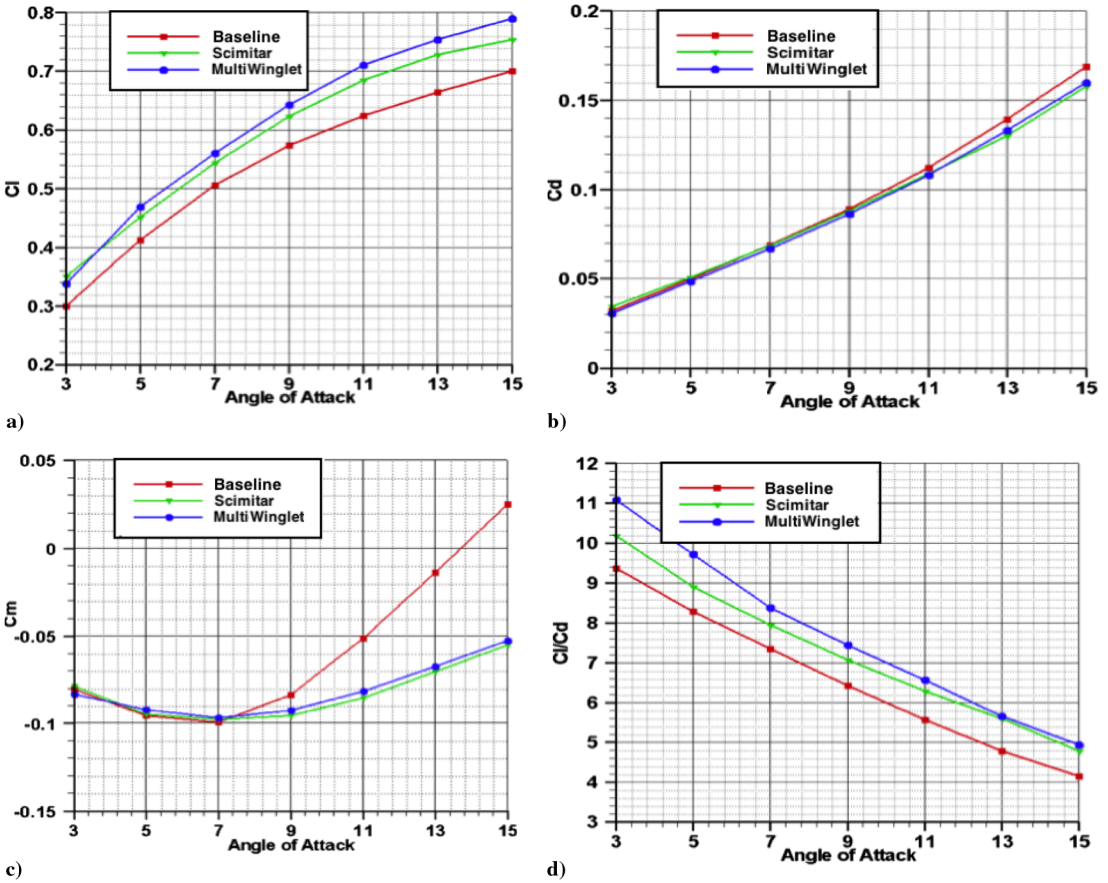

Fig. 11 Variations of a) C_l vs α, b) C_d vs α, c) C_m vs α, and d) C_l/C_d vs α for the baseline wing, optimized split-scimitar winglet and Pareto 4213 optimized three-element winglet.

Table 4 Aerodynamic coefficients for four configurations analyzed at Mach 0.8 and a 5 deg angle of attack

Winglet configuration	C_l	C_d	C_m
Baseline wing	0.330	0.0481	−0.085
Optimized blended winglet	0.340	0.0474	−0.083
Optimized split-scimitar winglet	0.360	0.0470	−0.080
Optimized three-element winglet	0.376	0.0465	−0.081

passenger aircraft. The temperature, density, viscosity, and pressure values at an altitude of 35,000 ft above sea level were incorporated into the model to account for the realistic cruise conditions. It can be seen that the optimized multi-element winglets still offered a larger reduction in drag and an increase in lift than the other two winglet configurations, although these improvements were not as large as in case of takeoff (Table 3). Please notice that these results at transonic speeds were obtained for the winglets that were optimized for takeoff low-speed conditions, not for transonic cruise conditions. Further improvements are possible by optimizing winglets for both flight regimes.

VII. Conclusions

This paper investigated the effectiveness of the multi-element winglet (mimicking bird wing-tip feathers) configuration to reduce the induced aerodynamic drag using a three-dimensional, compressible, steady-state Reynolds-averaged Navier–Stokes (RANS) equations solver in the OpenFOAM software suite. Multi-objective optimization was performed on the multi-element winglet configuration using the modeFRONTIER optimization software. The span, leading-edge and trailing-edge sweeps, cant angle, twist angle, and relative thickness of each of the three elements were used to parameterize the geometry. The four simultaneous objectives were to maximize coefficients of the lift and lift-to-drag ratio while minimizing the coefficients of the drag and pitching moment.

A multidimensional response surface was created using the Gaussian Radial Basis Function for each of the four objectives as a means to quickly evaluate the objective functions of any virtual geometric design. The response surface was then coupled with a genetic algorithm (NSGA-II) to arrive at a Pareto frontier. Five virtual designs were selected at random from the Pareto frontier and analyzed using a RANS solver. The interpolated objective function values from the response surface were in good agreement with those obtained from the RANS solver. The values of the geometric parameters of five designs were perturbed to simulate manufacturing defects. The Pareto 4213 geometry aerodynamic performance was least sensitive to geometric defects and was selected as the Pareto optimum design of choice. The computational results demonstrate that the multi-element winglet configuration offers a significant increase in the lift coefficient and a reduction in the induced drag and pitching moment. Such winglets diffused the vortex core more effectively than other winglet configurations. That is, the Pareto-optimized three-element winglet configuration allowed each element to influence the flow pattern due to the preceding elements.

Although this multi-element winglet concept has resulted in an increase in aerodynamic performance, greater caution should be taken if more winglet elements are to be added in a single wing-tip root, which might lead to the individual elements becoming thinner and more delicate. Therefore, a multidisciplinary multi-objective optimization must be performed to couple aerodynamic analysis with structural analysis.

Acknowledgments

The authors gratefully acknowledge the Florida International University Instructional and Research Computing Center for providing High Performance Computing resources used in this project. The authors would also like to express their appreciation to Carlo Poloni, Founder and President of ESTECO, for providing modeFRONTIER optimization software free of charge for this project.

References

[1] Hossain, A., Rahman, A., Hossen, J., Iqbal, P., Shaari, N., and Sivraj, G. K., "Drag Reduction in a Wing Model Using a Bird Feather Like Winglet," *Jordan Journal of Mechanical and Industrial Engineering*, Vol. 52, No. 6, June 2011, pp. 24–29.

[2] McCormick, B. W., *Aerodynamics of V/STOL Flight*, Academic Press, London, 1967, Chap. 4.

[3] Alford, L. D., Jr., and Clayman, G. J., Jr., U.S. Patent Application for "Blended Winglet," Docket No. 7,644,892, filed Jan. 2010.

[4] Reddy, S. R., Sobieczky, H., Abdoli, A., and Dulikravich, G. S., "Winglets: Multiobjective Optimization of Aerodynamic Shapes," *11th World Congress on Computational Mechanics*, edited by Oñate, E., Oliver, J., and Huerta, A., July 2014, Paper 2781.

[5] Reddy, S. R., Neiss, A., and Powell, S., "Design, Analysis and Multi-Objective Constrained Optimization of Multi-Winglets," Bachelor's Thesis, Mechanical and Materials Engineering Dept., Florida International Univ., Miami, FL, April 2014.

[6] Louis, B. G., U.S. Patent Application for "Spiroid-Tipped Wing," Docket No. 102,068, filed April 1992.

[7] Cosin, R., Catalano, F. M., and Correa, L. G. N., "Aerodynamic Analysis of Multi-Winglets for Low Speed Aircraft," *27th International Congress of the Aeronautical Sciences*, edited by Mari, C., Monclar, P., and Gabaldi, L., Sept. 2010, Paper ICAS2010-P2.15.

[8] Ceron-Munoz, H. D., and Catalano, F. M., "Experimental Analysis of the Aerodynamic Characteristics Adaptive of Multi-Winglets," *Proceedings of the Institution of Mechanical Engineers, Part G: Journal of Aerospace Engineering*, Vol. 220, No. 6, 2006, pp. 209–215. doi:10.1243/09544100JAERO22

[9] Kubrynski, K., "Wing-Winglet Design Methodology for Low Speed Applications," *41st Aerospace Science Meeting and Exhibit*, AIAA Paper 2003-0215, Jan. 2003.

[10] Tanenaka, K., Hatanaka, K., and Nakahashi, K., "Multi-Disciplinary Design Exploration for Winglet," *26th International Congress of the Aeronautical Sciences*, edited by Ying, S., and Bengelink, R., Sept. 2008, Paper ICAS2011-P2.46.

[11] Ursache, N. M., Melinm, T., Isikveren, A. T., and Friswell, M. I., "Morphing Winglets for Aircraft Multi-Phase Improvements," *7th AIAA Aviation Technology, Integration and Operations Conference*, AIAA Paper 2007-7813, Sept. 2007.

[12] Minella, G., Ugas, A., and Rodriguez, Y., "Aerodynamic Shape Design Optimization of Airplane Winglets," Bachelor's Thesis, Mechanical and Materials Engineering Dept., Florida International Univ., Miami, FL, Dec. 2010.

[13] Weierman, J., and Jacob, J. D., "Winglet Design and Optimization for UAVs," *AIAA Applied Aerodynamics Conference*, AIAA Paper 2010-4224, 2010.

[14] Cella, U., and Romano, D. G., "Assessment of Optimization Algorithms for Winglet Design," *EnginSoft-Newsletter Year 7nl*, EnginSoft, U.K., 2010.

[15] Bourdin, P., Gatto, A., and Friswell, M. I., "The Application of Variable Cant Angle Winglets for Morphing Aircraft Control," *24th AIAA Applied Aerodynamics Conference*, AIAA Paper 2006-3660, June 2006.

[16] Gavrilovic, N. N., Rasuo, B. P., Dulikravich, G. S., and Parezanovic, V., "Commercial Aircraft Performance Improvement by Using Winglets," *FME Transactions*, Vol. 43, No. 1, Jan. 2015, pp. 1–8.

[17] "OpenFOAM, Open Source Field Operation and Manipulation, Software Package, Ver. 2.2.0," OpenCFD, Ltd., Paris, 2000, http://www.opencfd.co.uk/openfoam/.

[18] "modeFRONTIER, Software Package, Ver. 4.5.4," ESTECO, Trieste, Italy, 2014.

[19] Colaco, J. M., and Dulikravich, G. S., "A Survey of Basic Deterministic, Heuristic and Hybrid Methods for Single-Objective Optimization and Response Surface Generation," *Thermal Measurements and Inverse Techniques*, edited by Orlande, H. R. B., Fudym, O., Milet, D., and Cotta, R., Taylor and Francis, Philadelphia, May 2011, pp. 355–405, Chap. 10.

[20] Klein, M., and Sobieczky, H., "Sensitivity of Aerodynamic Optimization to Parameterized Target Functions," *Inverse Problems in Engineering Mechanics*, edited by Tanaka, M., and Dulikravich, G. S., Elsevier Science, Oxford, 2001, pp. 1–10.

[21] Sobieczky, H., "Geometry Generator for CFD and Applied Aerodynamics," *New Design Concepts for High Speed Air Transport*, CISM Courses and Lectures No. 366, Springer–Verlag, New York, 1997, pp. 137–157.

[22] Rahman, U. A., and Mustapha, F., "Validations of OpenFoam Steady State Compressible Solver Rhosimplefoam," *International Conference on Mechanical and Industrial Engineering*, Kuala Lumpur, Malaysia,

Feb. 2015.
doi:10.15242/IAE.IAE0215214
[23] Ashrafi, Z. N., and Sedghat, A., "Improving the Aerodynamic Performance of a Wing with Winglet," *International Journal of Natural and Engineering Sciences*, Vol. 8, No. 6, 2014, pp. 52–57.
[24] Deb, K., Pratap, A., Agarwal, S., and Meyarivan, T., "A Fast and Elitist Multi-Objective Genetic Algorithm: NSGA-II," KanGAL Rept. 2000001, 2000.
[25] Deb, K., and Agarwal, R. B., "Simulated Binary Crossover for Continuous Search Space," *Complex Systems*, Vol. 9, No. 2, 1995, pp. 115–148.
[26] Sobol, I. M., "Distribution of Points in a Cube and Approximate Evaluation of Integrals," *U.S.S.R. Computational Mathematics and Mathematical Physics*, Vol. 7, No. 4, 1967, pp. 86–112.
doi:10.1016/0041-5553(67)90144-9